Electrohydrodynamic rotations of a viscous droplet

Paul F. Salipante and Petia M. Vlahovska

School of Engineering, Brown University, Providence, Rhode Island 02912, USA

We report a fluid system which exhibits chaotic dynamics under creeping flow conditions. A droplet in a uniform dc electric field deforms into an ellipsoid that can undergo irregular rotational motions. The nonlinear drop electrohydrodynamics is explained by a theoretical model which includes anisotropy in the polarization relaxation due to drop asphericity and charge convection due to rotational drop flow.

I. MOTIVATION

Nonlinear phenomena such as chaotic flows are not very common in the absence of inertia. Since the Stokes equations governing the fluid flow are linear, evolving boundary characteristics, e.g., shape, charge, and surfactant coverage, provide a possible source of nonlinearity [1]. For example, a single particle exhibits complex dynamics if it is deformable: a capsule or a red blood cell in shear flow [2–6] or a drop in oscillatory strain-dominated linear flows [7].

If the particle is rigid, a time-dependent induced surface charge can give rise to nonlinear dynamics [8–10]. Indeed, a sphere in a uniform electric field can undergo chaotic rotations [11,12], but only if particle inertia is not negligible. In the inertialess limit, anisotropic polarization relaxation (e.g., due to nonspherical particle shape) can become a source of chaotic particle tumbling [13,14], but such behavior has not been experimentally observed and remains an open question.

In this paper, we explore the effect of particle asphericity and fluidity on the electro-rotation dynamics. Upon application of a uniform direct current (dc) electric field, a neutral leaky-dielectric drop initially deforms into an ellipsoid, which then can exhibit unsteady motions, some of which are illustrated in Figs. 1 and 2. If the drop viscosity is high, the ellipsoid tumbles [see Fig. 1(b)], while randomly reversing its direction of rotation [15]. A low-viscosity drop however can undergo additional deformation while rotating [see Fig. 1(a)]. The resulting shape variations resemble oscillations and can have periodically modulated amplitudes [see Fig. 2(b)].

II. PHYSICAL PICTURE

When placed in an electric field, a particle polarizes because free charges carried by conduction accumulate at boundaries that separate media with different electric properties. It is instructive first to discuss the simplest example of a rigid sphere in a uniform electric field. The magnitude and orientation of the induced dipole depend on the mismatch of electric properties between the particle ("in") and the suspending fluid ("ex"), $R = \sigma_{\rm in}/\sigma_{\rm ex}$, $S = \epsilon_{\rm in}/\epsilon_{\rm ex}$, where σ and ϵ denote the conductivity and dielectric constant, respectively. The ratio of R to S compares the charge relaxation times of the media [16,17],

$$R/S = \frac{\tau_{c,\rm ex}}{\tau_{c,\rm in}}, \quad \text{where} \quad \tau_{c,\rm in} = \frac{\epsilon_{\rm in}}{\sigma_{\rm in}}, \ \tau_{c,\rm ex} = \frac{\epsilon_{\rm ex}}{\sigma_{\rm ex}}. \quad (1)$$

If $R/S < 1$ ($\tau_{c,\rm in} > \tau_{c,\rm ex}$), the conduction response of the exterior fluid is faster than that of the particle material. As

a result, the induced dipole is oriented opposite to the applied electric field direction. This configuration is unfavorable and becomes unstable above a critical strength of the electric field [11,18,19]. A perturbation in the dipole alignment gives rise to a torque, which drives physical rotation of the sphere. The induced surface-charge distribution rotates with the particle, but at the same time the exterior fluid recharges the interface. The balance between charge convection by rotation and supply by conduction from the bulk results in an oblique dipole orientation. In the inertialess limit, the rotation rate ω is determined from the balance of electric and viscous torques acting on the particle, $\mathbf{P} \times \mathbf{E} = \mathbf{A} \cdot \boldsymbol{\omega}$, where $\mathbf{A}$ is the friction matrix.

The spontaneous spinning of a rigid sphere in a uniform dc electric field is the classic Quincke electrorotation. In this case, the friction matrix is diagonal, and a straightforward calculation [18–20], assuming instantaneous polarization, yields three possible solutions: no rotation, $\Omega = 0$, and

$$\Omega = \pm \frac{1}{\tau_{\rm mw}} \sqrt{\frac{E_0^2}{E_Q^2} - 1}, \quad (2)$$

where the $\pm$ sign reflects the two possible directions of rotation and

$$\tau_{\rm mw} = \frac{\epsilon_{\rm in} + 2\epsilon_{\rm ex}}{\sigma_{\rm in} + 2\sigma_{\rm ex}} \quad \text{and} \quad E_Q^2 = \frac{2\sigma_{\rm ex}\mu_{\rm ex}(R+2)^2}{3\epsilon_{\rm ex}\epsilon_{\rm in}(1-R/S)}. \quad (3)$$

E_0 is the magnitude of the applied electric field. $\tau_{\rm mw}$, the Maxwell-Wagner polarization time, is the characteristic time scale for polarization relaxation. Notably, in Quincke rotation the dipole "tilt" is steady.

If sphere inertia and polarization relaxation, i.e., noninstantaneous charging of the interface described by $\partial_t \mathbf{P} = \boldsymbol{\Omega} \times \mathbf{P} - \tau_{\rm mw}^{-1}(\mathbf{P} - \mathbf{P}_{\rm eq})$, are included in the analysis, the polarization evolution equations and the torque balance map onto the Lorenz chaos equations [11,12]. As a result, in stronger fields the sphere may exhibit chaotic reversal of the rotation direction. For our experimental system, $E_Q = 2.7$ kV/cm and $E_{\rm chaos} \gtrsim 20E_Q$. The threshold for the chaotic rotations is significantly higher than experimentally observed, suggesting different origin of the unsteady rotations in our case.

Unlike solid particles, drops are fluid and have a free boundary. The electric stress deforms the drop and, as a result, the friction matrix and polarization relaxation become anisotropic and dependent on drop orientation relative to the applied electric field. In this paper we study the consequences of drop deformability on its Quincke-type rotational dynamics. Our previous work showed that at field strengths slightly above E_Q the electrorotational flow can lead to steady tilt of the
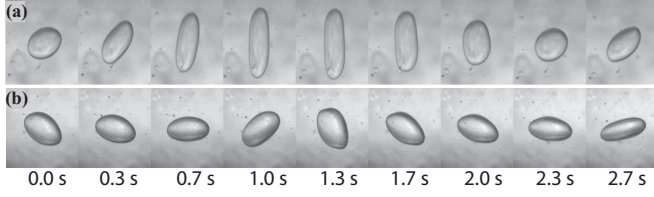
FIG. 1. Examples of unsteady drop behavior in a uniform dc electric field. (a) Viscosity ratio $\lambda = 1$, field strength $E_0 = 9.9$ kV/cm, drop radius $a = 1.8$ mm. (b) $\lambda = 14$, $E_0 = 9.7$ kV/cm, $a = 3.0$ mm.

ellipsoidal drop relative to the electric field [21]. In the present study we explore drop behavior in stronger fields.

III. EXPERIMENTAL METHODS

A. Fluid system

Silicone oil (SO) and castor oil (CO) (Alfa Aesar) are used as drop and suspending fluids, respectively. Both fluids
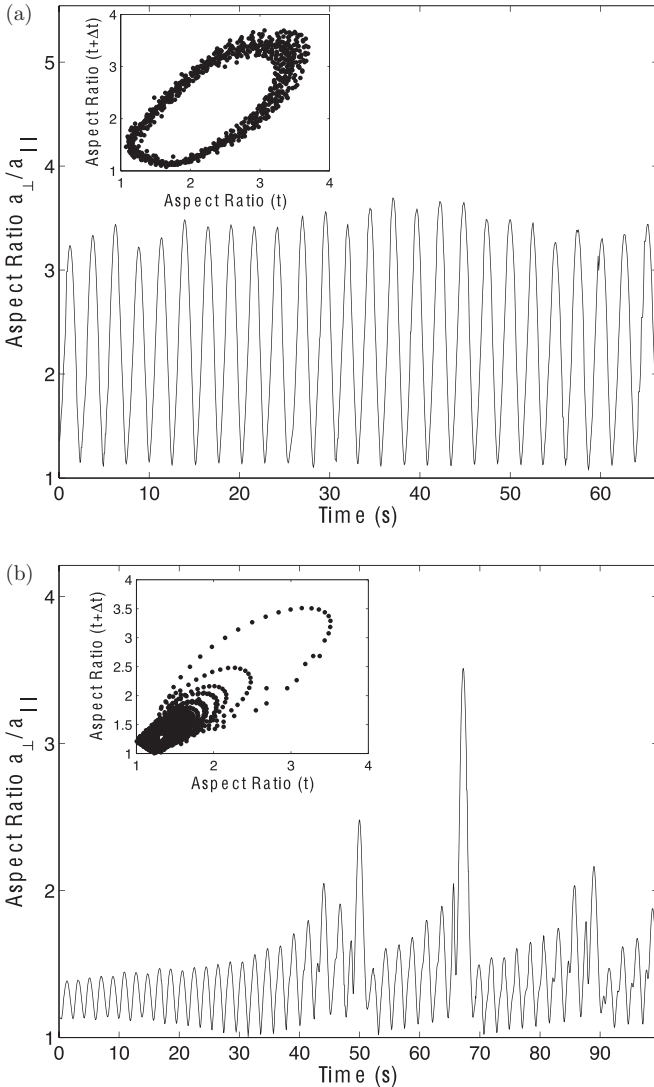

FIG. 2. Unsteady electrohydrodynamics of a droplet characterized by the evolution of the aspect ratio in real time (a),(b) and in time-delay plots with $\Delta t = 1/3$ s (insets). The viscosity ratios are $\lambda = 1$ for (a) and $\lambda = 4$ for (b).

have very low conductivity (in the order of 10^{-12} S/m) and very high viscosity (100 to 1000 times that of water). CO has $\mu_{ex} = 961$ Pa s and the SO viscosity is varied to adjust the viscosity ratio $\lambda = \mu_{in}/\mu_{ex}$ in the range between 0.1 to 14. The total electrical resistance of the fluid-filled chamber, measured with a sensitive Ohmmeter, is used to determine the fluid conductivity. Similarly, the capacitance of a fluid-filled chamber is measured to determine permittivity. The surface tension is measured to be 4.5 mN/m using the pendant drop method. For this system, the conductivity and permittivity ratios are $R = 0.027$ and $S = 0.56$.

B. Experimental setup and procedure

A uniform electric field is generated in a parallel-plate chamber constructed from transparent polymethylmethacrylate. The electrodes are two 5×5 cm^2 brass plates attached to the chamber walls. Chambers with different electrode distances, 1 and 2.5 cm, are used in order to observe a wide range of drop sizes and field strengths. The electric field is produced with a high-voltage dc amplifier (Ultravolt 40A-12) powered by a two-output power supply (Agilent E3646A). The amplifier is inside a sealed plastic box and is connected to the chamber with a high-voltage-rated wire. The output from the amplifier was verified using a Fluke air cleaner probe (80K-15) connected to a Fluke 115 multimeter.

In the experiment, a millimeter-sized drop is pipetted manually into the middle of the chamber, far away from any boundary. The field is then turned on and the voltage is increased stepwise in increments of approximately 300 V/cm; at each step the system is allowed to equilibrate in order to avoid spurious transients.

Video recordings of unsteady drop behavior are taken with a CCD camera (ThorLabs) at 15 frames per second. The chamber is aligned with the camera such that the electric field is oriented from bottom to top in the image. Video is recorded until the drop sediments to the bottom of the chamber, approximately 2–5 min, depending on the size of the drop.

The images are processed using image processing software, IMAGEJ. A pixel intensity threshold is taken on a stack of images to provide an outline of the drop interface. The image is converted to binary and the shape enclosed by the interface is converted to black. The shape is then analyzed using the built-in IMAGEJ algorithm "fit ellipse," which determines the major and minor axes and angle of inclination of the fitted ellipse. The drop deformation is determined by the ratio of the axes parallel and perpendicular to the axis of symmetry,

$$\beta = \frac{a_{\parallel}}{a_{\perp}}. \tag{4}$$

Once rotation begins, the true drop shape becomes a general ellipsoid and β is then determined from the drop contour in the plane of observation.

Note that the observation axis does not always coincide with the axis of drop rotation. The rotation axis can assume any direction perpendicular to the electric field and its orientation is not known *a priori*. For measurements of the drop angle, recordings were made when the drop tilted within the viewing plane, i.e., at an angle that is observable from the camera.

To verify that the chamber remains at room temperature, the amount of Ohmic heating resulting from electric current through the chamber is estimated. The highest voltage used is approximately 20 kV. The conductivity of the castor oil, $\sigma_{ex} = 4.5 \times 10^{-11}$ S/m, yields a resistance of approximately 100 MΩ for an area of 0.0025 m^2 and a gap of 2 cm. This yields a current across the chamber of 0.1 μA. This current gives a total energy input of 1 J over an estimated time of 1000 s. Using properties of castor oil, the mass of the chamber is estimated to be 0.05 kg and the heat capacity is $c_p \sim 1$ J/kg T. The change in temperature is estimated to be 0.01 K. The low amount of current through the chamber makes the Ohmic heating negligible over the duration of an experiment.

IV. TIME SCALES AND DIMENSIONLESS NUMBERS

In addition to the mismatch of electric properties R and S, defined by Eq. (1), the drop response to an electric field depends on the viscosity contrast between the drop and suspending fluids (which quantifies the drop "fluidity"),

$$\lambda = \frac{\mu_{in}}{\mu_{ex}}. \tag{5}$$

The accumulation of charge on the interface creates an electric stress, which drives the fluid motion. The resulting linear flow has a straining component, with characteristic time scale

$$\tau_{hd} = \frac{\mu_{ex}(1 + \lambda)}{\epsilon_{ex} E_0^2}, \tag{6}$$

and, above the threshold for Quincke rotation, a rotational component with characteristic time scale set by Eq. (2). Comparison of the flow time scale Eq. (6) (in the absence of electrorortation) or Eq. (2) (in the Quincke regime) to the inertia time scale $a^2 \rho_{ex}/\mu_{ex}(1 + \lambda)$, shows that the Reynolds number for the system is of the order of 10^{-3} and the observed phenomena occur in the Stokes flow regime.

Drop deformation is opposed by the interfacial tension γ, which acts to minimize the interfacial area of the drop. The characteristic time scale for a deformed drop to relax to its equilibrium spherical shape is given by

$$\tau_\gamma = \frac{\mu_{ex}(1 + \lambda)a}{\gamma}. \tag{7}$$

Note that the strength of the straining flow, characterized by Eq. (6), and the surface-tension-driven relaxation Eq. (7) depend on the viscosity ratio while the rotational flow, characterized by the Quincke rotation rate Eq. (2), is independent of viscosity ratio. This suggests that the dynamics of very viscous drops is dominated by rotation and shape variations will be negligible. In contrast, fluid systems for which the time scales are comparable are expected to display richer dynamics, since the drop deforms while rotating. This is indeed the case for drops with $\lambda = 1$, where all time scales are of the order of 1 s.

V. RESULTS

A. Experiment

Figure 3 summarizes the observed drop dynamics as a function of field strength, drop size, and viscosity ratio between the drop and suspending fluids.
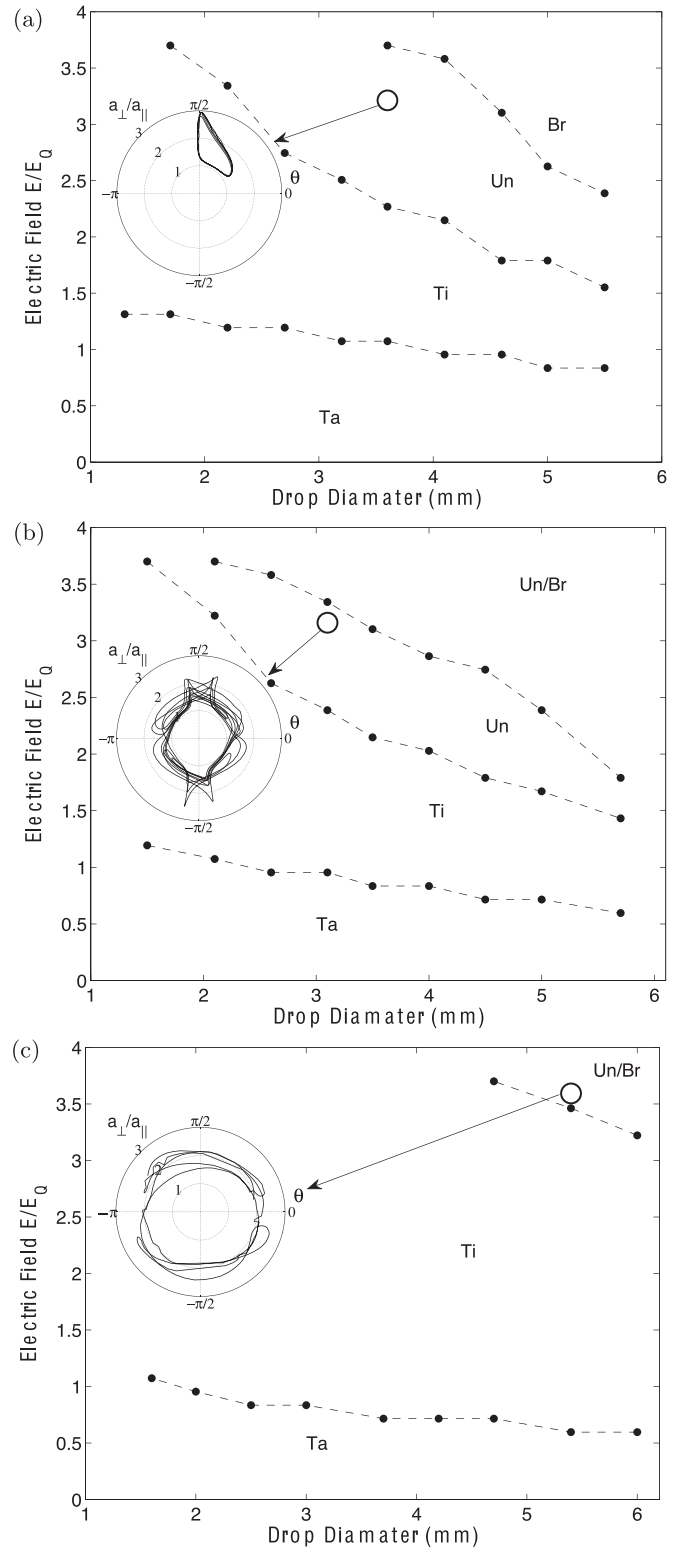

FIG. 3. Phase diagrams for viscosity ratios $\lambda = 1$ (a), 4 (b), and 14 (c). Taylor (Ta) indicates axisymmetric straining flow and oblate deformation, Ti a steady tilted drop orientation with rotational flow, unsteady (Un) a time-dependent drop shape and orientation, and Br drop breakup. The inset shows the time-dependent behavior for one drop indicated on the chart with ◦ in terms of the variations of the aspect ratio β (concentric circles) with the major axis orientation relative to the applied electric field θ. E_Q, given by Eq. (3), is the critical electric field for rotation of a sphere.
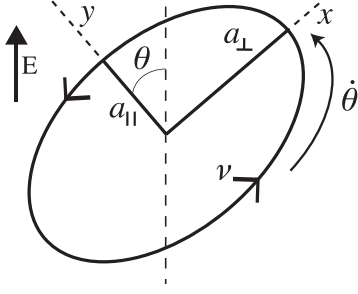
FIG. 4. Sketch of the "fluid ellipsoid" model for drop electrorotation. Drop asphericity is characterized by the aspect ratio $\beta = a_\parallel / a_\perp$. The rigid body rotation is related to the tilt angle of the deformed shape, θ, by $\dot\theta = d\theta/dt$. In the corotating frame the interface velocity is $v(-y\beta, x/\beta)$.

In weak fields, the drop becomes an oblate spheroid, which is axisymmetrically aligned with the applied field (the classic Taylor regime [22]). In stronger fields, the drop assumes a steady oblique orientation relative to the field direction [21]. Further increase in the field strength leads to a variety of unsteady dynamics or drop breakup (for videos see [15]). High-viscosity drops ($\lambda = 14$) tumble while reversing their rotation direction irregularly. In contrast, low-viscosity drops ($\lambda = 1$) undergo undamped shape oscillations with steady amplitude. Intermediate-viscosity drops ($\lambda = 4$) exhibit a mix of both behaviors, namely, repeated cycles consisting of shape oscillations with increasing amplitude followed by several tumbles in random directions. These behaviors are better seen in the insets of Fig. 3, in which the trajectories in the (β, θ) phase space are plotted; θ is the angle between the drop major axis and the applied field direction and β is the aspect ratio; see Fig. 4 for a sketch of the geometry. The shape variations are due to periodic drop stretching and compression by the electric stresses (which are time dependent in the drop corotating frame) and should not be confused with the Rayleigh oscillations of an inviscid drop [23].

B. Model

The tumbling motion of a highly viscous drop can be analyzed by modeling the drop as an ellipsoid with fixed shape. Next we develop an analytical model which builds upon the one for a rigid ellipsoid by Cebers *et al.* [14] modified to account for the fluid motion inside the drop. Including shape variations as seen in the case of lower-viscosity drops is challenging and possible only in numerical simulations.

For simplicity, the ellipsoid is assumed to be an axisymmetric oblate spheroid with aspect ratio set by the drop elongation when rotation is initiated. The torque balance is

$$\alpha_\perp \left(\frac{d\theta}{dt} + \frac{2\beta}{1+\beta^2} v \right) = P_\parallel E_\perp - P_\perp E_\parallel + (\chi_\parallel^\infty - \chi_\perp^\infty) E_\perp E_\parallel,$$

(8)

where $\alpha_\perp$ is the friction coefficient [defined by Eq. (A11)], χ^∞ is the high-frequency susceptibility [given by Eq. (A13)], and $\parallel, \perp$ denote components parallel and perpendicular to the axis of symmetry; see Fig. 4. The rotational fluid motion inside the drop is characterized by a frequency v. The latter is determined from the balance of electrical energy input and

viscous dissipation, in a similar fashion to the analysis of drop rotation in a magnetic field [24], or red blood cell tank treading in shear flow [25]. Details of the calculations are provided in the Appendix. The polarization relaxation equations in a coordinate system rotating with $\dot\theta$ are

$$\frac{\partial P_\parallel}{\partial t} = -v P_\perp \beta - \frac{1}{\tau_\parallel}[P_\parallel - (\chi_\parallel^0 - \chi_\parallel^\infty)E_\parallel],$$

(9a)

$$\frac{\partial P_\perp}{\partial t} = \frac{v P_\parallel}{\beta} - \frac{1}{\tau_\perp}[P_\perp - (\chi_\perp^0 - \chi_\perp^\infty)E_\perp],$$

(9b)

where $\tau_{\parallel,\perp}$ and $\chi_{\parallel,\perp}^0$ are the directional (β-dependent) Maxwell-Wagner relaxation time scales and low-frequency susceptibility respectively, defined by Eqs. (A15) and (A14). If $v = 0$, Eqs. (8) and (9) reduce to the equations of motion for a rigid ellipsoid [14], and predict three types of behavior: alignment of the long axis with the electric field, oscillations around the field direction ("swinging"), and continuous flipping ("tumbling"). The additional torque associated with the fluid rotation inside the drop (characterized by v) changes fundamentally the response of the oblate ellipsoid to the electric field: the long axis can be either perpendicular or tilted to the field direction.

Thus a fluid ellipsoid exhibits more behaviors: steady axisymmetric orientation with long axis perpendicular to the applied field (Taylor regime), steady tilted orientation, swinging around a nonzero tilt angle with respect to the electric field, and tumbling. Moreover, chaotic switching between the swinging and tumbling states is also found. The model highlights that in all cases except for the chaotic behavior, the motion of the dipole mirrors the motion of the ellipsoid. Chaotic motion is associated with a lack of synchronization between the ellipsoid and dipole orientations.

C. Comparison between theory and experiment

The model captures the dynamics of the high-viscosity drops, as seen from Fig. 5, with no adjustable parameters. The
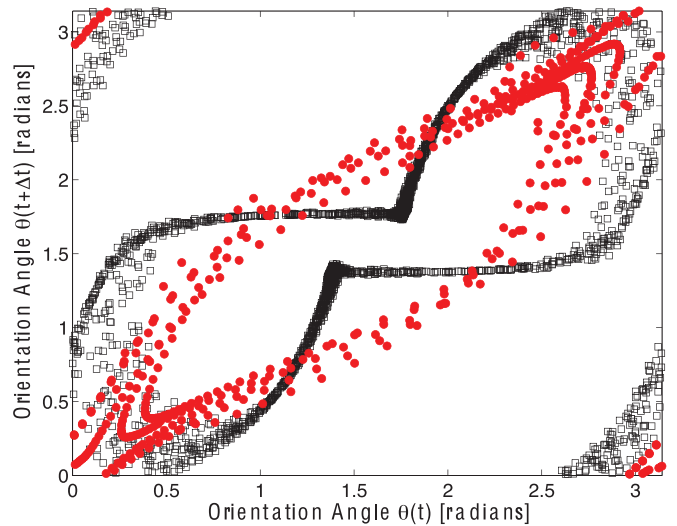

FIG. 5. (Color online) Delay plots for the orientation angle for a $\lambda = 14$, $2a = 6.9$ mm drop in an electric field with strength $E_0 = 9.1$ kV/cm ($3.1 E_Q$) from the experiment [red (light gray)] and the model (black).
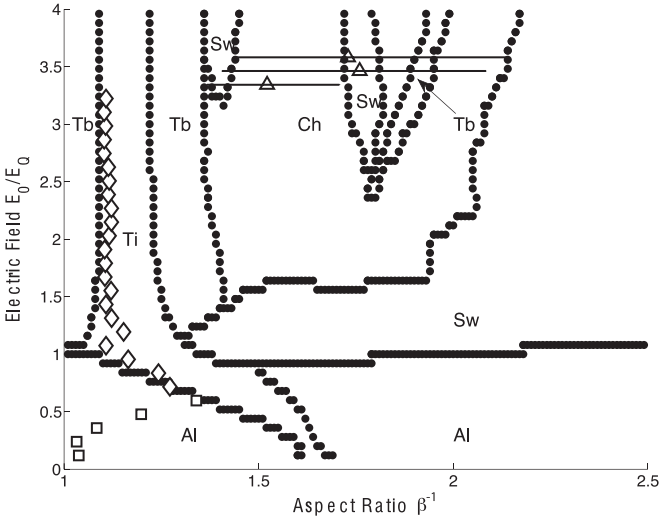
FIG. 6. Phase diagram for a fluid ellipsoid with viscosity ratio $\lambda \equiv \mu_{in}/\mu_{ex} = 14$. The lines represent the boundaries between various behaviors computed from the model: Taylor (Al), steady tilt (Ti), swinging (Sw), tumbling (Tb), and chaotic rotations (Ch). The symbols correspond to experimental data: $\square$, Taylor regime, $\diamond$, steady tilted ellipsoid, and $\triangle$, chaotic tumbling. The lines crossing the symbols reflect the variations in the aspect ratio of the drop during rotation.

phase diagram resulting from the numerical solution of Eq. (8) and Eq. (9) is shown in Fig. 6, and compares qualitatively well to the results of experiments.

Of course in reality the drop shape does not remain an ellipsoid with fixed aspect ratio, as seen from Fig. 2. The experiments show variations in the drop elongation; the range of aspect ratios experienced by a drop during one cycle is indicated by a line crossing the symbols in Fig. 6. The shape oscillations are more pronounced in the case of low-viscosity drops [see Figs. 1(a), 2(a), and 3(a)]. However, the main axis is found to oscillate around a defined tilted angle and hence this behavior qualitatively corresponds to the swinging mode.

Shape variations are due to comparable time scales of rotation Ω^{-1} [which in turn depends on the Maxwell-Wagner polarization time τ_{mw}; see Eq. (2)], deformation by electric stresses $\mu_{ex}(1+\lambda)/\epsilon_{ex}E_0^2$, and relaxation driven by the interfacial tension γ, $a\mu_{ex}(1+\lambda)/\gamma$; all are about 1 s for $\lambda = 1$. In the case of $\lambda = 14$, the rotation rate is an order of magnitude shorter than the time scales for shape change, which justifies the assumption of a fixed shape in our model. Modeling the drop deformation is a challenging task which can be accomplished only numerically in a three-dimensional code. A recent analytical work based on a small-deformation theory failed to predict the undamped shape oscillations of the electrorotating drop [26].

VI. CONCLUSIONS

We report unsteady dynamics of a viscous droplet in uniform dc electric fields. Depending on the viscosity ratio between the drop and suspending fluid, the droplet can chaotically tumble, undergo oscillatory deformations, or show a mix of both behaviors. Our finding is a rare example of chaos under creeping flow conditions and could inspire additional approaches to small-scale fluid mixing and electromanipulation of particle motion in microfluidic technologies. Intriguingly, similar electrorotation behavior has been displayed by vesicles (closed biomimetic membranes) [27], which hints that the findings in this work may have relevance to a broader range of soft particles such as capsules and biological cells. Finally, many particle interactions modify the Quincke behavior [28] and could also give rise to interesting nonlinear dynamics.

APPENDIX: MODEL DETAILS

The fluid inside the ellipsoidal drop undergoes rotational flow with frequency ν; see Fig. 4. The interface velocity $\mathbf{u}_s = \nu(-y\beta, x/\beta)$ (in the corotating frame) affects the torque balance and the polarization relaxation equations. The torque due to the rotational flow is identical to that developed for the tank-treading interface on a red blood cell in shear flow [25]. The surface flow also contributes to charge convection, which modifies the polarization relaxation equations.

The shape-preserving fluid flow inside the ellipsoid is given by [29]

$$\mathbf{u}^{in} = \nu\left(-y\beta, \frac{x}{\beta}, 0\right). \tag{A1}$$

At distances far from the fluid drop, the the fluid undergoes rotational motion with frequency set by the frequency of the tumbling ellipsoid $\dot{\theta}$,

$$\mathbf{u}^{ex} = -\dot{\boldsymbol{\theta}} \times \mathbf{r} = (y\dot{\theta}, -x\dot{\theta}, 0). \tag{A2}$$

The external field can be written in terms of the internal field plus a disturbance field $\mathbf{u}^D$ as

$$\mathbf{u}^{ex} = \mathbf{u}^{in} + \mathbf{u}^D. \tag{A3}$$

At $r \to \infty$, the velocity fields must match; this gives

$$\mathbf{u}^D = \left(y(\dot{\theta} + \nu\beta), -x\left(\dot{\theta} + \nu\frac{1}{\beta}\right), 0\right). \tag{A4}$$

The velocity-gradient tensor can be decomposed as

$$\lim_{r \to \infty} \frac{\partial \mathbf{u}_i^D}{\partial x_j} = \gamma_{ij} + \omega_{ij}, \tag{A5}$$

with symmetric and antisymmetric components γ_{ij} and ω_{ij}, respectively. For the case of an ellipsoid, the tensor components are

$$\gamma_{12} = \gamma_{21} = \frac{\nu}{2}\left(\beta - \frac{1}{\beta}\right),$$
$$\omega_{12} = -\omega_{21} = \dot{\theta} + \frac{\nu}{2}\left(\beta + \frac{1}{\beta}\right). \tag{A6}$$

A torque from the flow field is produced by the combined effects of surface flow and rigid body rotation. The magnitude of this torque is given by [30]

$$L_{TT+TB} = V\mu_{ex}(A_{21} - A_{12}), \tag{A7}$$

where μ_{ex} is the external fluid viscosity, V is the volume of the ellipsoid, and

$$A_{12} = 2\frac{n_{\|}\gamma_{12} + n_3'\omega_{12}}{(\beta^2 n_{\|} + n_{\perp})n_3'},$$

$$A_{21} = 2\frac{n_{\perp}\gamma_{21} + \beta^2 n_3'\omega_{21}}{(\beta^2 n_{\|} + n_{\perp})n_3'}, \quad \text{(A8)}$$

$$n_3' = -\frac{n_{\|} - n_{\perp}}{\beta^2 - 1},$$

where $n_{\|,\perp}$ are shape factors which for oblate ellipsoids ($\beta < 1$) are

$$n_{\|} = \frac{1+e^2}{e^3}(e - \text{arctanh}(e)), \quad \text{where} \quad e = \sqrt{1/\beta^2 - 1}. \quad \text{(A9)}$$

and the second shape factor is $n_{\perp} = (1 - n_{\|})/2$.

Combining the expressions in Eq. (A6) into Eq. (A7), the torque simplifies to the expression,

$$L_{TT+TB} = -\alpha_{\perp}\left(\dot{\theta} + \frac{2\beta}{1+\beta^2}\nu\right), \quad \text{(A10)}$$

where $\alpha_{\perp}$ is the friction coefficient

$$\alpha_{\perp} = 2\mu_{ex}V M_{\perp}, \quad M_{\perp} = \frac{1+\beta^2}{\frac{1-n_{\|}}{2} + n_{\|}\beta^2}. \quad \text{(A11)}$$

The electric torque on an ellipsoid in a uniform electric fields is given by

$$\mathbf{L}_E = \mathbf{P}_T \times \mathbf{E}. \quad \text{(A12)}$$

Note that total polarization is $P_T = P + P_{\infty}$, and $P_{\infty} = \chi^{\infty}E$ is the instantaneous polarization.

In the viscosity-dominated limit, where particle inertia is negligible, the conservation of angular momentum reduces to $L_{TT+TB} + L_E = 0$, i.e., Eq. (8). The polarization relaxation equations which describe the time-dependent interfacial charging are given by Eq. (9) in a frame of reference corotating with the ellipsoid. In these evolution equations

$$\chi_{\|,\perp}^{\infty} = \frac{\epsilon_{ex}V(\epsilon_{in} - \epsilon_{ex})}{(\epsilon_{in} - \epsilon_{ex})n_{\|,\perp} + \epsilon_{ex}} \quad \text{(A13)}$$

are the high-frequency directional susceptibilities, and $E_{\|} = E_0 \cos\theta$ and $E_{\perp} = -E_0 \sin\theta$.

$$\chi_{\|,\perp}^0 = \frac{\epsilon_{ex}V(\sigma_{in} - \sigma_{ex})}{(\sigma_{in} - \sigma_{ex})n_{\|,\perp} + \sigma_{ex}} \quad \text{(A14)}$$

are the low-frequency susceptibilities and

$$\tau_{\|,\perp} = \frac{(\epsilon_{in} - \epsilon_{ex})n_{\|,\perp} + \epsilon_{ex}}{(\sigma_{in} - \sigma_{ex})n_{\|,\perp} + \sigma_{ex}} \quad \text{(A15)}$$

are the directional Maxwell-Wagner relaxation times.

Equations (8) and (9) are nondimensionalized before solving. The variables are normalized by

$$\tilde{t} = \frac{t}{\tau_{mw}}, \quad \tilde{P} = \frac{P}{P_c},$$

$$\tilde{L}_E = \frac{L_E}{P_c E_0}, \quad \tilde{\nu} = \nu\tau_{mw}, \quad \text{(A16)}$$

$$P_c = \Delta\chi_s\epsilon_{ex}E_0 V, \quad \Delta\chi_s = \frac{9(R-S)}{(R+2)(S+2)}. \quad \text{(A17)}$$

In dimensionless form, the torque balance equation (8) becomes

$$\dot{\theta} = -\frac{2\beta}{1+\beta^2}\tilde{\nu} + \frac{BC_1}{2M_{\perp}}[(-\tilde{P}_{\perp}\cos\theta - \tilde{P}_{\|}\sin\theta) - C_2\cos\theta\sin\theta], \quad \text{(A18)}$$

where

$$B = \frac{\epsilon_{ex}^2 E_0^2}{\mu_{ex}\sigma_{ex}}, \quad C_1 = \frac{9(R-S)}{(R+2)^2},$$

$$C_2 = \left[\frac{(S-1)}{(S-1)n_{\|}+1} - \frac{(S-1)}{(S-1)n_{\perp}+1}\right]\left(\frac{S+2}{R+2}\right). \quad \text{(A19)}$$

The dimensionless polarization relaxation equations are

$$\frac{\partial \tilde{P}_{\|}}{\partial \tilde{t}} = -\tilde{\nu}\tilde{P}_{\perp}\beta - T_{\|}(\tilde{P}_{\|} - X_{\|}\cos\theta), \quad \text{(A20a)}$$

$$\frac{\partial \tilde{P}_{\perp}}{\partial \tilde{t}} = \frac{\tilde{\nu}\tilde{P}_{\|}}{\beta} - T_{\perp}(\tilde{P}_{\perp} + X_{\perp}\sin\theta), \quad \text{(A20b)}$$

where

$$T_{\|,\perp} = \frac{\tau_{mw}}{\tau_{\|,\perp}} = \left(\frac{S+2}{R+2}\right)\left(\frac{(R-1)n_{\|,\perp}+1}{(S-1)n_{\|,\perp}+1}\right) \quad \text{(A21)}$$

and

$$X_{\|,\perp} = \frac{(R+2)(S+2)}{9[1+n_{\|,\perp}(R-1)][1+n_{\|,\perp}(S-1)]}. \quad \text{(A22)}$$

The final variable to be determined is the surface-flow frequency ν, which is found by balancing the rate of electrical energy input with viscous dissipation. The viscous dissipation, first derived by Keller and Skalak [25], is given by

$$\Pi_{TT+TB} = (\mu_{in} - \mu_{ex})\nu^2 V\left(\frac{1}{\beta} - \beta\right)^2 + \mu_{ex}\nu V\left(\beta A_{12} - \frac{1}{\beta}A_{21}\right). \quad \text{(A23)}$$

Taking into account Eq. (A10) the above equation reduces to

$$\Pi_{TT+TB} = \mu_{ex}\nu^2 V(\lambda f_1 - f_2) + \frac{4\nu L_E}{M_{\perp}\left(\beta n_{\|} + \frac{1}{\beta}n_{\perp}\right)}, \quad \text{(A24)}$$

where

$$f_1 = (\beta - 1/\beta)^2, \quad f_2 = f_1\left[1 - \left(\frac{\beta^2-1}{(n_{\|}-n_{\perp})(\beta^2+1)}\right)\right]. \quad \text{(A25)}$$

The energy input from the electric field, Π_E, is determined by the surface integral,

$$\Pi_E = \int \mathbf{u}_s \cdot (\underline{\underline{\mathbf{T}}}^{el} \cdot \hat{\mathbf{n}})dS, \quad \text{(A26)}$$

where $\underline{\underline{\mathbf{T}}}^{el}$ is the Maxwell stress. Using the definitions for the surface flow and Maxwell stress, the rate of work done by the

electric stresses is expressed as

$$\mathbf{u}_s \cdot (\underline{\underline{\mathbf{T}}}^{\text{el}} \cdot \hat{\mathbf{n}}) = \frac{1}{V} \nu (\mathbf{E}^d \cdot \hat{\mathbf{t}})(\mathbf{P} \cdot \hat{\mathbf{n}}), \tag{A27}$$

where $\mathbf{E}^d$ is the electric field inside the drop. The electric field in an ellipsoid is given by [20,31]

$$E_{\parallel,\perp}^d = E_{\parallel,\perp}^\infty - \frac{n_{\parallel,\perp}}{\epsilon_{\text{ex}} V}(P_{\parallel,\perp} + P_{\parallel,\perp}^\infty), \tag{A28}$$

where $E_{\parallel,\perp}^\infty$ is the electric field at infinity and $P_{\parallel,\perp} + P_{\parallel,\perp}^\infty$ is the total polarization in component form. The exact expressions in the integral Eq. (A26) are

$$\mathbf{E}^d \cdot \hat{\mathbf{t}} = -\beta E_\parallel^d y + \frac{1}{\beta} E_\perp^d x, \quad \mathbf{P} \cdot \hat{\mathbf{n}} = P_\parallel n_\parallel + P_\perp n_\perp. \tag{A29}$$

Equation (A26) is integrated using Eq. (A28), Eq. (A29), and the relation $\int dS r_i n_k = V \delta_{ik}$, leading to

$$\Pi_E = \nu \left(-\beta E_\parallel^d P_\perp + \frac{1}{\beta} E_\perp^d P_\parallel \right). \tag{A30}$$

Nondimensionalizing using the same parameters from Eqs. (A16) and (A17) yields

$$\Pi_E = \epsilon_{\text{ex}} E_0^2 V \nu \Delta\chi_s \left(-\beta[\cos\theta - n_\parallel \Delta\chi_s(\tilde{P}_\parallel + C_3 \cos\theta)]\tilde{P}_\perp \right.$$
$$\left. + \frac{1}{\beta}[-\sin\theta - n_\perp \Delta\chi_s(\tilde{P}_\perp - C_4 \sin\theta)]\tilde{P}_\parallel \right), \tag{A31}$$

where

$$C_3 = \frac{\chi_\parallel^\infty}{\epsilon_{\text{ex}} V \Delta\chi_s}, \quad C_4 = \frac{\chi_\perp^\infty}{\epsilon_{\text{ex}} V \Delta\chi_s}. \tag{A32}$$

Setting this expression equal to $\Pi_{\text{TT+TB}}$ and solving for $\tilde{\nu}$ gives a lengthy expression for the surface-flow frequency,

$$\tilde{\nu} = \frac{BC_1}{\lambda f_1 - f_2} \left[\frac{-2}{\left(\beta n_\parallel + \frac{n_\perp}{\beta}\right)M_\perp} \right.$$
$$\times (\tilde{P}_\parallel \sin\theta + \tilde{P}_\perp \cos\theta + C_2 \cos\theta \sin\theta)$$
$$- \beta[(\cos\theta - n_\parallel \Delta\chi_s(\tilde{P}_\parallel + C_3 \cos\theta)]\tilde{P}_\perp$$
$$\left. + \frac{1}{\beta}[-\sin\theta - n_\perp \Delta\chi_s(\tilde{P}_\perp - C_4 \sin\theta)]\tilde{P}_\parallel \right]. \tag{A33}$$

The final equations describing the fluid ellipsoid in an electric field are given in dimensionless form as

$$\frac{\partial\theta}{\partial\tilde{t}} = -\frac{2\beta}{1+\beta^2}\tilde{\nu} + \frac{B}{2M_\perp}[C_1(-\tilde{P}_\perp \cos\theta - \tilde{P}_\parallel \sin\theta)$$
$$- C_2 \cos\theta \sin\theta], \tag{A34}$$

$$\frac{\partial\tilde{P}_\parallel}{\partial\tilde{t}} = -\tilde{\nu}\tilde{P}_\perp\beta - T_\parallel(\tilde{P}_\parallel - X_\parallel \cos\theta), \tag{A35a}$$

$$\frac{\partial\tilde{P}_\perp}{\partial\tilde{t}} = \frac{\tilde{\nu}\tilde{P}_\parallel}{\beta} - T_\perp(\tilde{P}_\perp + X_\perp \sin\theta). \tag{A35b}$$

[1] J. Błgawzdziewicz, R. H. Goodman, K. Khurana, E. Wajnryb, and Y.-N. Young, Physica D **239**, 1214 (2010).

[2] T. Omori, Y. Imai, T. Yamaguchi, and T. Ishikawa, Phys. Rev. Lett. **108**, 138102 (2012).

[3] T. Gao, H. H. Hu, and P. P. Castaneda, Phys. Rev. Lett. **108**, 058302 (2012).

[4] J. M. Skotheim and T. W. Secomb, Phys. Rev. Lett. **98**, 078301 (2007).

[5] J. Dupire, M. Abkarian, and A. Viallat, Phys. Rev. Lett. **104**, 168101 (2010).

[6] P. M. Vlahovska, Y-N. Young, G. Danker, and C. Misbah, J. Fluid. Mech. **678**, 221 (2011).

[7] Y.-N. Young, J. Błgawzdziewicz, V. Cristini, and R. H. Goodman, J. Fluid Mech. **607**, 209 (2008).

[8] T. Ward and G. M. Homsy, J. Fluid Mech. **547**, 215 (2006).

[9] G. Yossifon, I. Frankel, and T. Miloh, Phys. Fluids **19**, 068105 (2007).

[10] Y. Dolinsky and T. Elperin, Phys. Rev. E **80**, 066607 (2009).

[11] E. Lemaire and L. Lobry, Physica A **314**, 663 (2002).

[12] F. Peters, L. Lobry, and E. Lemaire, Chaos **15**, 013102 (2005).

[13] A. Cebers, J. Magn. Magn. Mater. **122**, 277 (1993).

[14] A. Cebers, E. Lemaire, and L. Lobry, Phys. Rev. E **63**, 016301 (2000).

[15] See Supplemental Material at http://link.aps.org/supplemental/10.1103/PhysRevE.88.043003 for movies.

[16] J. R. Melcher and G. I. Taylor, Annu. Rev. Fluid Mech. **1**, 111 (1969).

[17] D. A. Saville, Annu. Rev. Fluid Mech. **29**, 27 (1997).

[18] T. B. Jones, IEEE Trans. Indust. Appl. **IA-20**, 845 (1984).

[19] I. Turcu, J. Phys. A **20**, 3301 (1987).

[20] T. B. Jones, *Electromechanics of Particles* (Cambridge University Press, New York, 1995).

[21] P. F. Salipante and P. M. Vlahovska, Phys. Fluids **22**, 112110 (2010).

[22] G. I. Taylor, Proc. R. Soc. London, Ser. A **291**, 159 (1966).

[23] O. A. Basaran, J. Fluid. Mech. **241**, 169 (1992).

[24] A. V. Lebedev, A. Engel, K. I. Morozov, and H. Bauke, New J. Phys. **5**, 57 (2003).

[25] S. R. Keller and R. Skalak, J. Fluid Mech. **120**, 27 (1982).

[26] H. He, P. F. Salipante, and P. M. Vlahovska, Phys. Fluids **25**, 032106 (2013).

[27] P. F. Salipante, R. L. Knorr, R. Dimova, and P. M. Vlahovska, Soft Matter **8**, 3810 (2012).

[28] D. Das and D. Saintillan Phys. Rev. E **87**, 043014 (2013).

[29] G. B. Jeffery, Proc. R. Soc. London, Ser. A **102**, 161 (1922).

[30] A. Engel, A. V. Lebedev, and K. I. Morozov, Z. Naturforsch. **58a**, 703 (2003).

[31] E. M. Lifshitz, L. D. Landau, and L. P. Pitaevskii, *Electrodynamics of Continuous Media* (Butterworth-Heinemann, London, 1984).